Facile Synthesis of Mn3O4−Reduced Graphene Oxide Hybrids for Catalytic Decomposition of Aqueous Organics

ARTICLE *in* INDUSTRIAL & ENGINEERING CHEMISTRY RESEARCH · FEBRUARY 2013

Impact Factor: 2.59 · DOI: 10.1021/ie303220x

5 AUTHORS, INCLUDING:

Yunjin Yao
Hefei University of Technology
25 PUBLICATIONS **804** CITATIONS
SEE PROFILE

Shaoming Yu
Hefei University of Technology
26 PUBLICATIONS **617** CITATIONS
SEE PROFILE

Shaobin Wang
Curtin University
271 PUBLICATIONS **9,327** CITATIONS
SEE PROFILE

I&EC research
Industrial & Engineering Chemistry Research

Article

pubs.acs.org/IECR

Facile Synthesis of Mn_3O_4–Reduced Graphene Oxide Hybrids for Catalytic Decomposition of Aqueous Organics

Yunjin Yao,*[,†,‡,§] Chuan Xu,[†,‡] Shaoming Yu,[†,‡] Dawei Zhang,[†,‡] and Shaobin Wang*[,§]

[†]School of Chemical Engineering, Hefei University of Technology, Hefei 230009, People's Republic of China
[‡]Anhui Key Laboratory of Controllable Chemical Reaction & Material Chemical Engineering, Hefei 230009, China
[§]Department of Chemical Engineering, Curtin University, G.P.O. Box U1987, Perth, WA 6845, Australia

ABSTRACT: Mn_3O_4–reduced graphene oxide (rGO) hybrids were synthesized, and their catalytic performance in heterogeneous activation of peroxymonosulfate (PMS) to oxidize a target pollutant, Orange II, in aqueous solutions was investigated. The surface morphology and structure of the Mn_3O_4–rGO hybrids were characterized by field emission scanning electron microscopy (FESEM), energy-dispersive X-ray spectroscopy (EDS), transmission electron microscopy (TEM), powder X-ray diffraction (XRD), Raman spectroscopy, X-ray photoelectron spectroscopy (XPS), and thermogravimetric analysis (TGA). Through an in situ chemical deposition and reduction, Mn_3O_4–rGO hybrids with Mn_3O_4 nanoparticles at an average size of 29.2 nm were produced. The catalytic activity in Orange II oxidative decomposition was evaluated in view of the effects of various processes, pH, PMS concentration, Orange II concentration, and temperature. The combination of Mn_3O_4 nanoparticles with graphene sheets leads to a much higher catalytic activity than that of pure Mn_3O_4 or rGO. Graphene was found to play an important role in Mn_3O_4 dispersion and decomposition of Orange II. Typically, 30 mg/L of Orange II could be completely oxidized in 120 min at 25 °C and 0.05 g/L of Mn_3O_4–rGO hybrids, showing a promising application of the catalyst in the oxidative degradation of aqueous organic pollutants. The efficiency of Orange II decomposition increased with increasing temperature (25–55 °C), pH (4.0–11.0), and PMS dosage (0.25–1.5 g/L), but it decreased with increasing initial Orange II concentration (30–90 mg/L). Mn_3O_4–rGO hybrids exhibited stable performance without losing activity after four successive runs.

1. INTRODUCTION

Industrial processes generate increasing amounts of wastewater, containing toxic and hazardous organic compounds (such as dyes, pesticides, pharmaceuticals, etc.) that cause severe problems to the environment.[1,2] Recently, advanced oxidation processes (AOPs), involving various chemical, photocatalytic, electrocatalytic, and Fenton oxidation methods, have been intensively investigated because they can decompose organic pollutants to inorganic compounds such as H_2O, CO_2, and inorganic salts.[3−5] Among these AOPs, wet hydrogen peroxide catalytic oxidation is known as an efficient way, where $^{\bullet}OH$ is usually the main reactive and oxidizing species generated to degrade organic contaminants. However, this process has some drawbacks in cost-intensive production, transport and storage of H_2O_2, as well as pH adjustments.[6] Recently, sulfate radical ($SO_4^{-\bullet}$) initiators such as peroxymonosulfate (Oxone, PMS) have attracted increasing attention. PMS, a type of (bi) sulfite, has a higher oxidizing potential (1.82 V) than H_2O_2 (1.76 V), and is an inexpensive and environmentally friendly oxidant in several different applications, especially in chemically mineralizing various organic contaminants. In addition to high reactivity, its main advantage over H_2O_2 is easy handling as a solid.[7,8] In the past few years, several studies related to the activation of PMS have focused on transition metals, among which Co(II) and supported cobalt catalysts were found to be the best activators.[9−11] However, Co(II) is a highly toxic metal, which can induce some health problems.[9,12] Therefore, it remains a challenge to develop the transition metal catalysts to activate PMS as an environmentally friendly and applicable technology. Some attempts using less toxic Mn oxides have been reported.[13,14]

It is well-known that hausmannite (Mn_3O_4) has drawn particular research attention because of its distinctive structure and physicochemical properties, which are of great interest in energy conversion, magnetics, and catalysis, etc.[15,16] Despite the high catalytic performance of Mn_3O_4 nanoparticles (NPs), poor chemical and thermal stabilities of the material have led to aggregation of NPs, thus lowering the catalytic efficiency. To tackle with these issues, carbonaceous materials with high electrical conductivity and buffer matrix have been widely employed as matrixes for Mn_3O_4-based materials to improve their conductivity and stability.[17] As compared to other carbon matrixes such as graphite, carbon black, and carbon nanotubes, graphene is emerging as one of the most appealing carbon materials because of its unique properties such as superior electrical conductivity, excellent mechanical flexibility, and high thermal and chemical stabilities.[18,19] Because chemically modified graphene materials can exhibit enhanced performance, it has become a priority for researchers to prepare these hybrids with ZnO,[20,21] TiO_2,[22,23] $NiFe_2O_4$,[24] and $CoFe_2O_4$,[25] etc. Mn_3O_4–graphene hybrids have been recently prepared as anode and supercapacitor materials with performance comparable to that of previously reported Mn_3O_4-based ano-

Received: November 22, 2012
Revised: January 18, 2013
Accepted: January 25, 2013
Published: January 25, 2013

dx.doi.org/10.1021/ie303220x | *Ind. Eng. Chem. Res.* 2013, 52, 3637−3645

des.[15,26−28] However, to our best knowledge, little work has been done in catalytic reactions of Mn_3O_4−graphene hybrids, in particular, for the heterogeneous activation of PMS.

In this Article, we present a facile approach for preparing Mn_3O_4-reduced graphene oxide (rGO) under basic conditions and its application in catalytic oxidation of Orange II by PMS. The physical and chemical characterizations of Mn_3O_4−rGO hybrids were conducted, and the performance in heterogeneous reaction was evaluated in view of the effects of the main variables (e.g., solution pH, Orange II and PMS concentration, and temperature). The reaction kinetics, material stability, degradation mechanism, as well as the role of Mn_3O_4 and graphene were also studied. The as-prepared hybrids demonstrated high catalytic activities in wastewater treatment.

2. MATERIALS AND METHODS

2.1. Synthesis of Mn_3O_4−rGO Hybrids. Graphite oxide was synthesized by oxidation of graphite powder under acidic conditions according to the modified Hummers method as described elsewhere.[29−31] In a typical preparation of Mn_3O_4−rGO hybrids, 0.6 g of graphite oxide was dispersed in 250 mL of water by sonication for 2 h to achieve uniform dispersion of graphene oxide (GO), and 1.928 g of manganese acetate tetrahydrate ($Mn(C_2H_3O_2)_2{\cdot}4H_2O$) was dissolved in 20 mL of distilled water. Next, manganese acetate aqueous solution was added into the GO dispersion under vigorous magnetic stirring for 1 h, and NaOH aqueous solution (50%) was added dropwise to the above mixture to make solution pH > 10, followed by stirring of 4 h. Subsequently, 10 mL of hydrazine hydrate was added to the above solution, and the temperature of the solution was raised to 80 °C with constant stirring. After 5 h, the solution was cooled to room temperature, and the precipitate was collected by a centrifuge and rinsed thoroughly with deionized water and ethanol. Afterward, the obtained powders were dried at 60 °C overnight in a vacuum oven. For a comparison, bare Mn_3O_4 NPs and rGO nanosheets were also prepared in a similar procedure but without adding graphite oxide or $Mn(C_2H_3O_2)_2{\cdot}4H_2O$.[32,33] All of the products were stored in a desiccator for further experiments.

2.2. Catalyst Characterization. Powder X-ray diffraction (XRD) patterns of samples were recorded on a Bruker Advance D-8 diffractometer operated at a voltage of 40 kV and a current of 40 mA, using Cu Kα (λ = 1.5418 Å) radiation. Raman scattering was performed on a Dilor Labram model 1B dispersive Raman spectrometer using the helium−neon laser at 632.8 nm. X-ray photoelectron spectroscopy (XPS) was conducted using an ESCALAB250 spectrometer equipped with a monochromatized Al Kα source. The morphology of samples was investigated by field emission scanning electron microscopy (FESEM) (Zeiss Neon 40EsB FIBSEM) and transmission electron microscopy (TEM) (JEOL 2011 TEM) equipped with an energy-dispersive X-ray spectrometer (EDS). For TEM, a suspension of Mn_3O_4−rGO hybrids in ethanol was drop-casted onto carbon-coated copper grids and dried under ambient conditions. Thermogravimetric analysis (TGA) and differential thermal analysis (DTA) of samples were carried out on a Perkin-Elmer Diamond TG/DTA thermal analyzer in airflow at a rate of 100 mL/min. The surface areas of Mn_3O_4 and Mn_3O_4−rGO samples were 25.9 and 65.0 m^2/g, respectively, which were determined by N_2 adsorption isotherm using the BET method on a Coulter SA 3100 apparatus.

2.3. Catalyst Performance. The catalytic oxidation of Orange II was evaluated in a 300 mL glass beaker with a magnetic stirrer, heating jacket, and a condenser. The pH (pH_i) of the solution was initially adjusted to a desired value using NaOH or HNO_3 in all experiments. The pH (pH_o) after the reaction was further analyzed by a pH meter. A typical reaction mixture contained the following chemicals: (a) Orange II (30 mg/L, 200 mL); (b) Mn_3O_4−rGO (10 mg); and (c) oxidant Oxone (0.3 g). The reactions were carried out for various times, and aqueous phase samples (1.0 mL) were withdrawn at periodic intervals (up to 120 min) and immediately filtered (0.8 μm) to remove essentially the catalyst solids. Next, 1.0 mL of methanol was added to quench the reaction. Methanol is a well-known quenching agent, which reacts with $SO_4^{-\bullet}$ at high rates. The decolorization of Orange II was immediately inhibited after the addition of methanol.[34,35] Temporal concentration of dye in withdrawn samples was analyzed by UV/vis spectrophotometry at the maximum absorption band (484 nm). The reaction was also carried on at different temperatures (25, 35, 45, and 55 °C). Orange II was tested at four initial concentrations from 30 to 90 mg/L. Three different catalysts, rGO, Mn_3O_4, and Mn_3O_4−rGO, were used. Oxone was also used at several doses from 0 to 300 mg. In the stability tests of Mn_3O_4−rGO hybrids, the catalyst was gathered after completion of the reaction, washed, dried under vacuum, and reused in a fresh solution of Orange II and PMS.

3. RESULTS AND DISCUSSION

3.1. Catalyst Characterization. XRD patterns of Mn_3O_4−rGO hybrid before and after catalytic oxidation of Orange II are shown in Figure 1, together with as-prepared bare Mn_3O_4 NPs.

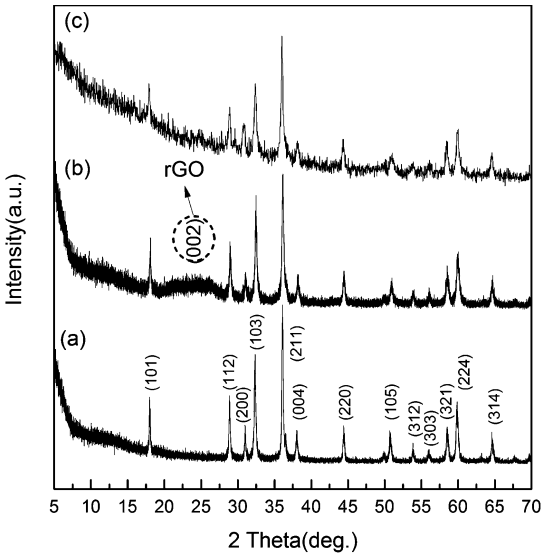

Figure 1. XRD patterns of Mn_3O_4 (a), and Mn_3O_4−rGO hybrid before (b) and after (c) catalytic oxidation of Orange II.

The positions and relative intensities of the peaks associated with Mn_3O_4−rGO hybrids and bare Mn_3O_4 are indexed perfectly as a pure Mn_3O_4 (hausmannite, space group: *I*41/*amd*) with lattice constants of $a = b = 5.763$ Å and $c = 9.456$ Å (JCPDS no. 89-4837), which matches well with previous reports.[15] As compared to pure Mn_3O_4 (Figure 1b), a weak broad diffraction (002) on Mn_3O_4−rGO appears at 2θ of 24.5−27.5°, which can be indexed to the disorderedly stacked graphene sheets.[15,36] In both samples, no impurities were detected in the XRD patterns, confirming the high purity of the

dx.doi.org/10.1021/ie303220x | Ind. Eng. Chem. Res. 2013, 52, 3637−3645

products. These results indicate that the as-synthesized hybrid consists of disorderedly stacked graphene and crystalline Mn_3O_4 NPs. The average crystallite size of Mn_3O_4 can be estimated from the Debye−Scherrer formula.[37] The average crystallite sizes of bare Mn_3O_4 and Mn_3O_4 in raw Mn_3O_4−rGO were 40.4 and 29.2 nm, respectively, which were consistent with the TEM observations (see Figure 4).

Raman spectroscopy is used for distinguishing ordered and disordered crystal structures of carbon. Figure 2 presents the Raman spectra of bare rGO and fresh Mn_3O_4−rGO hybrids. The G band (~1595 cm^{-1}) corresponding to sp^2-hybridized carbon and the D band (~1352 cm^{-1}) originating from disordered carbon are observed on both samples.[20] The intensity ratio of the D to the G band (I_D/I_G) provides a sensitive measure of the disorder and crystallite size of the graphitic layers. The intensity ratio (1.55) of I_D/I_G for rGO is closer to that (1.51) of Mn_3O_4−rGO hybrids, suggesting the reduction of exfoliated GO. In addition, the minor peaks of Raman shift at 659 cm^{-1} in Mn_3O_4−rGO hybrids can be attributed to the symmetric stretch of Mn_3O_4. These results confirm the existence of both graphene and Mn_3O_4 in the as-prepared hybrids.[38]

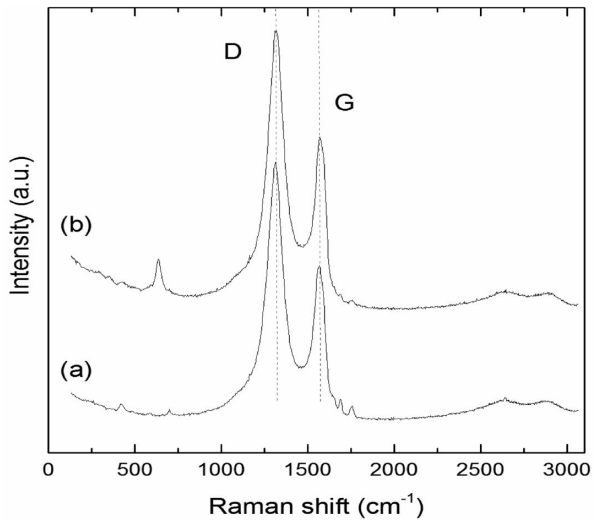

Figure 2. Raman spectra of (a) rGO and (b) Mn_3O_4−rGO.

The chemical bonding states in Mn_3O_4−rGO were further analyzed by XPS (Figure 3). In the survey region (0−1000 eV), carbon, manganese, and oxygen were detected. It was observed that there is an energy separation of 11.9 eV between Mn $2p_{1/2}$ and Mn $2p_{3/2}$ peaks in the Mn 2p region (Figure 3b), which is in accordance with the spectrum of Mn_3O_4.[15,28] The C 1s peak located at 284.58 eV is related to the graphitic carbon in graphene (Figure 3c). The O 1s XPS spectrum of the hybrid shows three different peaks centered at 530.0, 531.4, and 533.0 eV, which are corresponding to Mn−O−C bond, Mn−O−Mn bond, and Mn−O−H bond, respectively (Figure 3d).[39,40] These results are in good agreement with the XRD and Raman studies. The reduction of GO and restoration of the conjugated aromatic system guarantees good electronic conductivity, which makes graphene a good channel for electron transfer.[15]

FESEM and TEM images were collected for bare Mn_3O_4 NPs and Mn_3O_4−rGO hybrids, as shown in Figure 4. The bare

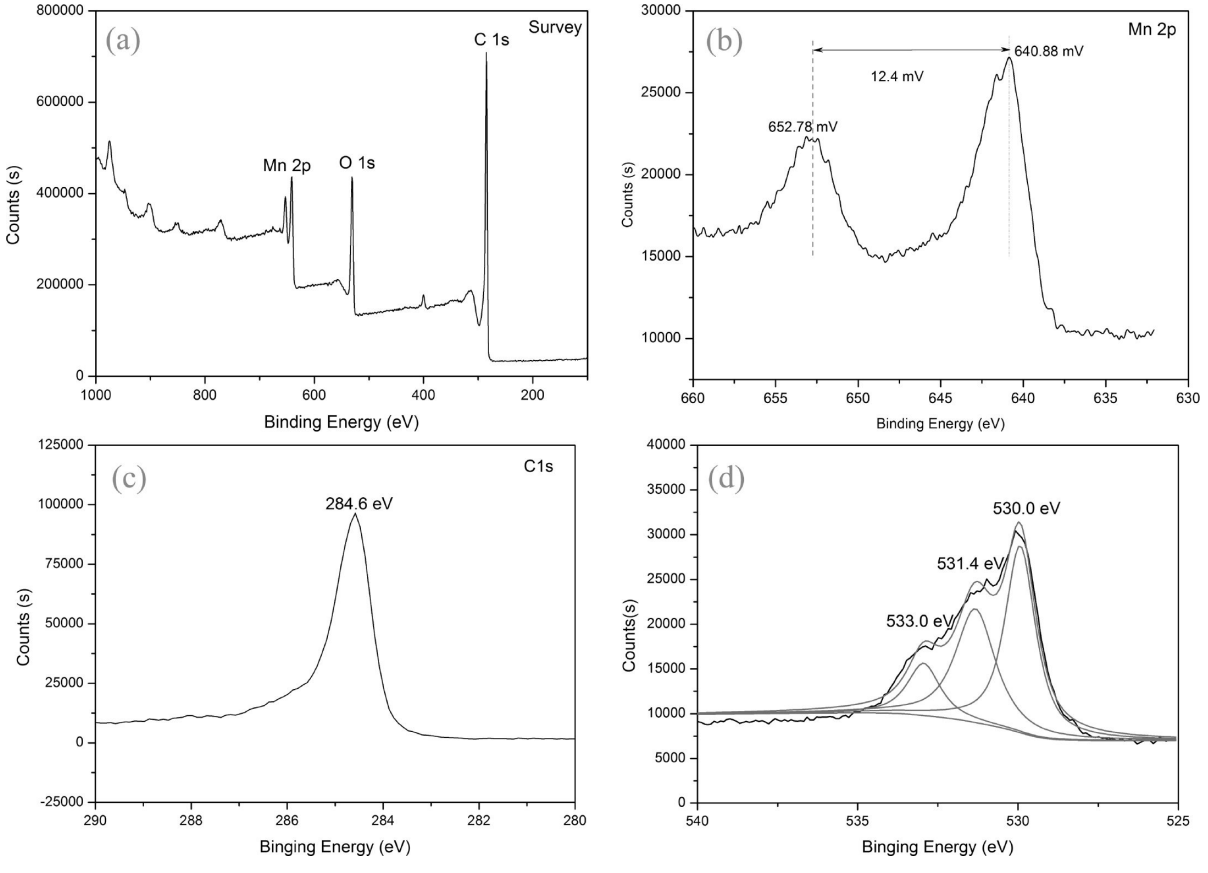

Figure 3. XPS spectra of Mn_3O_4−rGO: (a) survey scan; (b) Mn 2p region; (c) C 1s region; and (d) O 1s region.

dx.doi.org/10.1021/ie303220x | Ind. Eng. Chem. Res. 2013, 52, 3637−3645

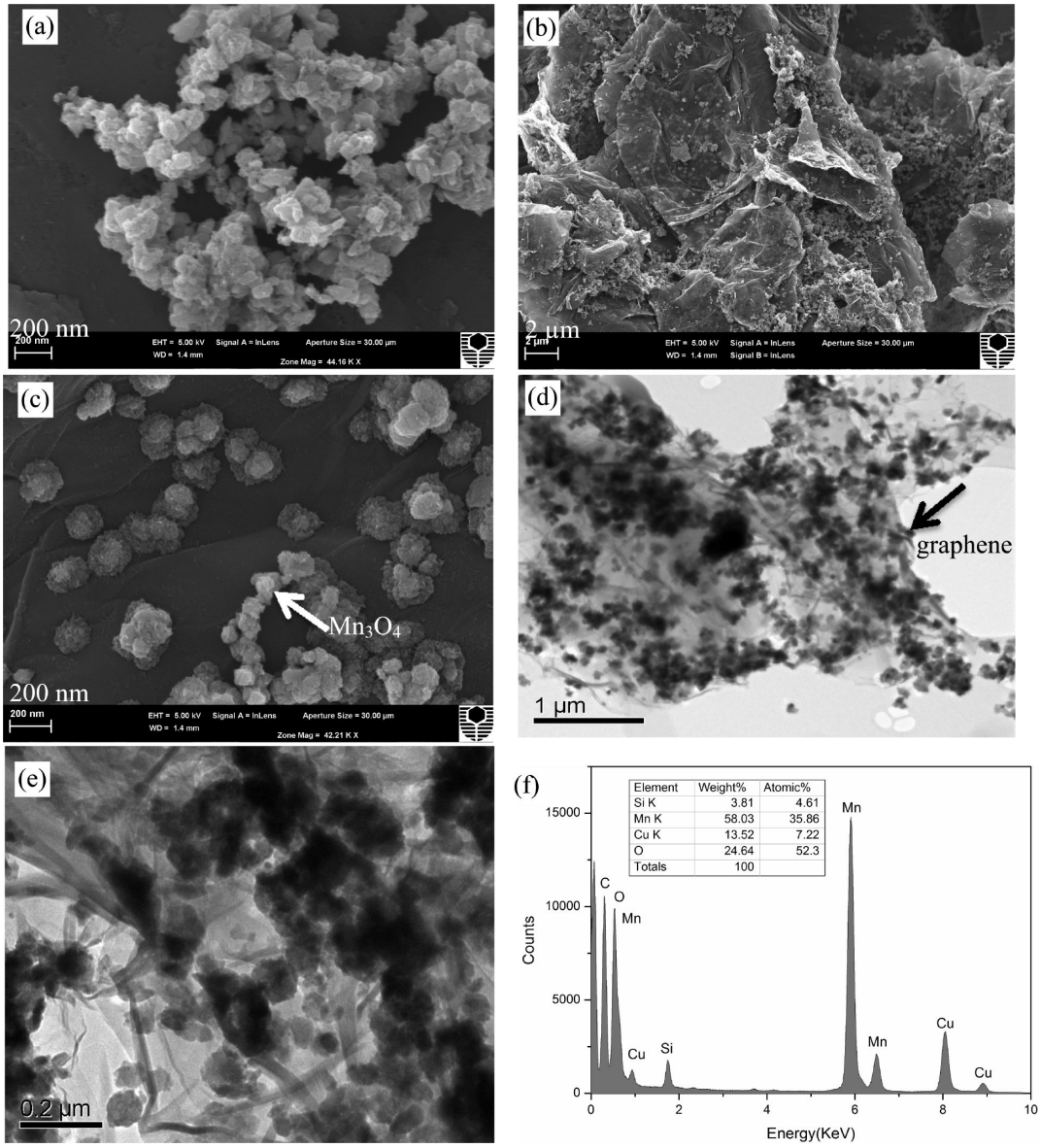

Figure 4. (a) SEM image of bare Mn_3O_4. (b–e) SEM and TEM images with different magnifications of Mn_3O_4–rGO hybrid. (f) EDS of the hybrid.

Mn_3O_4 NPs show as spherical particles, but the NPs are severely aggregated together, giving a bigger particle size in the range of 40–100 nm (Figure 4a). In comparison, the size of the Mn_3O_4 NPs in Mn_3O_4–rGO is around 29 nm (Figure 4b), which is consistent with the average particle size from XRD pattern (29.2 nm). This suggests that the intimate interaction between bare Mn_3O_4 NPs and hierarchic flexible graphene sheets drastically limits the agglomeration of the crystalline Mn_3O_4 NPs to some extents. Mn_3O_4 NPs were encapsulated in a matrix of graphene sheets, leading to more effective ionic and electron transport due to the high conductivity of graphene. TEM images (Figure 4c,d) further reveal that Mn_3O_4 NPs were distributed on the surface of graphene nanosheets in either single particle or small particle clusters. On the basis of the TEM images, it could be confirmed the presence of an intimate interaction between the Mn_3O_4 NPs and the graphene sheets, and such a combination enables fast electron transport through the graphene matrix to the Mn_3O_4 NPs, guaranteeing efficient chemical performance.[26] Both the TEM and the SEM images show the formation of thin rGO sheets.[20] EDS confirms the formation of a Mn_3O_4–rGO hybrid, where only Mn, O, and C elements on the rGO sheets can be detected with Cu and Si peaks emanating from the TEM grids (Figure 4f).

The thermal stability of rGO and Mn_3O_4–rGO hybrids has been studied by TG-DTA under airflow, as shown in Figure 5. Two distinct weight losses were observed on the TGA profile of rGO. An initial weight loss could be attributed to the removal of physically adsorbed water molecules below 120 °C. The gradual weight decrease in a temperature range of 120–460 °C could be attributed to the removal of the residual oxygenate groups on the surface of rGO. In the temperature range of 460–630 °C, a strong exothermic peak (594 °C) was observed in the DTA curve. This could be attributed to the burning of the carbon sketch of rGO.[41] However, for Mn_3O_4–rGO hybrids, the burning temperature of the carbon sketch was shifted to a lower value (422 °C), resulting from the catalytic effect of the manganese oxide.[42]

3.2. Catalytic Evaluation. Orange II is one of the representative organic dyes and has been widely applied in industrial production, which often contaminates the environ-

dx.doi.org/10.1021/ie303220x | Ind. Eng. Chem. Res. 2013, 52, 3637–3645

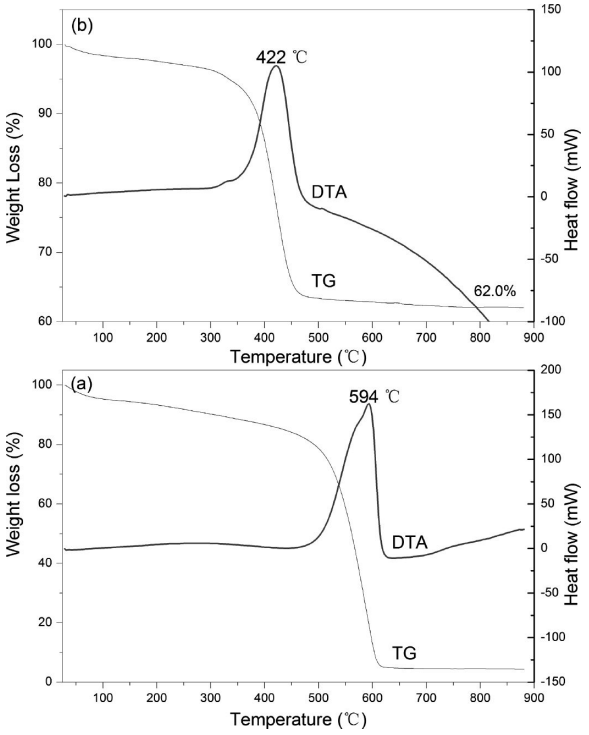

Figure 5. TG-DTA curves of (a) rGO and (b) Mn_3O_4–rGO.

ment. Figure 6a shows preliminary tests of adsorption and catalytic degradation of Orange II by Mn_3O_4, rGO, and Mn_3O_4–rGO hybrids in aqueous solution. The results show that Mn_3O_4, rGO, and Mn_3O_4–rGO are able to adsorb Orange II at low efficiency, which was negligible as compared to the fast removal of Orange II by heterogeneous catalytic reaction. Furthermore, in the presence of PMS, Mn_3O_4–rGO hybrids exhibited the highest catalytic activity among three catalysts: 100% of Orange II was degraded by the Mn_3O_4–rGO within 2 h under the same conditions. The color of Orange II solution gradually diminished upon $SO_4^{-\bullet}$ in the presence of Mn_3O_4–rGO hybrids, indicating that catalysis destroyed the chromophoric structure of the dye. On the contrary, the catalytic activities of pure Mn_3O_4 and graphene were much lower. For pure Mn_3O_4, 81.5% of Orange II was removed, while for graphene, the degradation of Orange II only reached 55% at 120 min, indicating that graphene is catalytically active. Previous investigations found that chemically reduced graphene oxide retains oxygen-containing groups such as ketonic (C═O) group at zigzag edges, which are rich in electrons, and thus has a great potential to coordinate a redox process.[43] Therefore, the combination of Mn_3O_4 and graphene results in a synergistic effect in catalytic activity, enhancing the relative rates of mass transfer and chemical reaction at reactive sites, which is similar to the systems of Co_3O_4–rGO,[44] $MnFe_2O_4$–rGO,[45] and $CoFe_2O_4$–rGO.[25]

Figure 6b depicts the representative UV–vis spectra during Orange II degradation by Mn_3O_4–rGO/PMS system. The main absorption band at 484 nm, corresponding to the n–p* transition of the azo form, and another band at 310 nm, attributed to the p–p* transition of the naphthalene ring, diminished simultaneously, indicating complete destruction of the azo and naphthalene structure of Orange II.[46,47] The absorption peak at 484 nm diminished with increasing reaction time, indicating that the rapid degradation of Orange II was attributed to the decomposition of the dye structure.

To go further in understanding the efficiency of Orange II degradation by Mn_3O_4–rGO/PMS system, the effects of different operating parameters, including initial solution pH, reaction temperature, and concentrations of PMS and Orange II, were investigated. The solution pH can remarkably influence pollutant degradation rate,[48] as presented in Figure 7a in a range of 4–11. About 64% of Orange II was reduced after 120 min of reaction at pH 4.0, and the degradation of Orange II was found to be enhanced significantly with the increase of solution pH. Zhu et al.[49] reported that the formation of Co–OH complexes at the surface of cobalt implanted TiO_2 nanoparticles was enhanced at the elevated pH value, which is the critical step for heterogeneous activation of PMS. A similar process for the formation of Mn–OH complexes at the surface of Mn_3O_4–rGO might occur, and more amounts of Mn–OH complexes were produced for PMS activation as pH increased from 4 to 11. Liang and Su[50] reported that the degradation of nitrobenzene was enhanced as pH increased from 7 to 12 in the thermally activated peroxodisulfate system. Hence, controlling pH could be considered as one approach to manipulate the degradation of pollutants in the $SO_4^{-\bullet}$ existing system.[48] It is

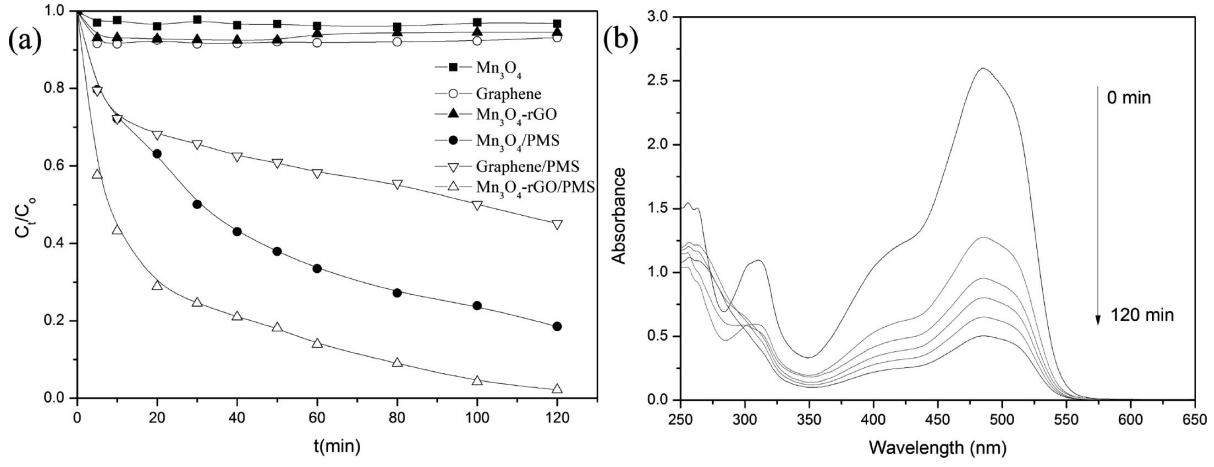

Figure 6. (a) Orange II degradation under different conditions. (b) UV–vis spectral changes for Orange II degradation with Mn_3O_4–rGO/PMS system (reaction conditions: [Orange II] = 30 mg/L, [PMS] = 0.3 g/200 mL, [catalyst] = 10 mg/200 mL, pH_i = 7.0, and T = 25 °C).

dx.doi.org/10.1021/ie303220x | Ind. Eng. Chem. Res. 2013, 52, 3637–3645

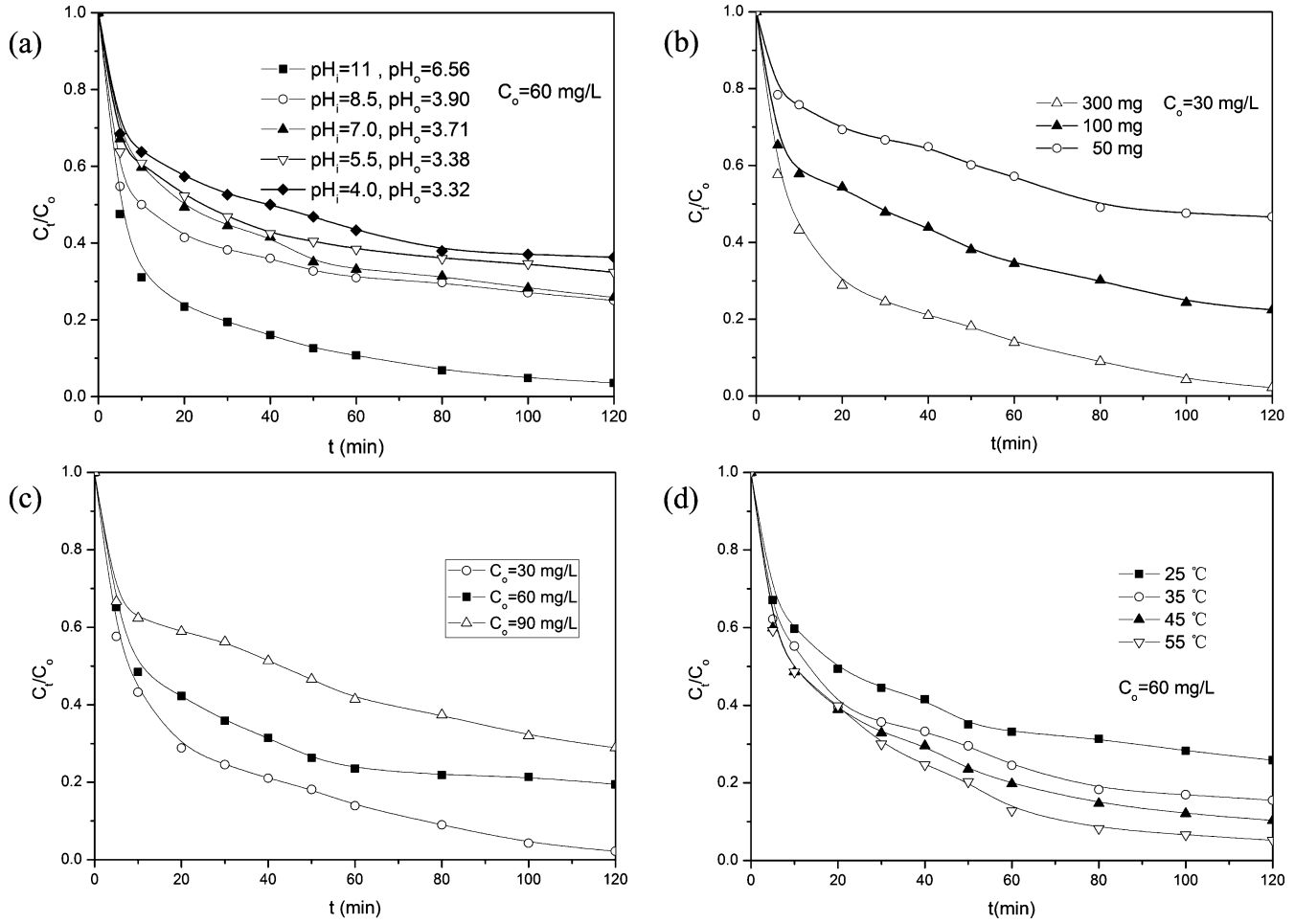

Figure 7. Factorial effects of heterogeneous reaction on Orange II degradation: (a) initial pH value, (b) PMS dosage, (c) initial Orange II concentration, and (d) reaction temperature. Except for the investigated parameter, other parameters were fixed: pH_i = 7.0, [PMS] = 0.30 g/200 mL, [Mn_3O_4−rGO] = 10 mg/200 mL, and T = 25 °C.

noted that the pH of solution after reaction was reduced, which was due to the formation of acid intermediates and carbonates.

The degradation of Orange II over Mn_3O_4−rGO/PMS was further studied at varying amounts of Oxone (Figure 7b) and initial Orange II concentrations (Figure 7c). Obviously, with an increase in Oxone dose (0.05, 0.1, and 0.3 g), the decomposition rate of Orange II was increasing. Increased doses of Oxone led to the time of Orange II decomposition reducing from 45 (at 0.05 g) to 30 min (at 0.3 g). Oxone is reacted with Mn^{2+} generating $SO_4^{-\bullet}$, and it can also react with Mn^{3+} to regenerate Mn^{2+} as in the Fenton-like reaction. The increase in Oxone dose would provide more chance to the reaction with Mn_3O_4−rGO, which enhances the rate of activation of PMS to generate $SO_4^{-\bullet}$, resulting in an increase in Orange II removal.

An increase in initial Orange II concentration, however, resulted in declined Orange II oxidation efficiency. The Orange II in the solution was completely removed within 120 min at the initial Orange II concentration of less than 30 mg/L, while about 61% of Orange II was removed within the same time at Orange II concentration of 90 mg/L. At the same concentrations of Mn_3O_4−rGO hybrids and PMS, a high amount of Orange II in solution will require more time to achieve the same removal rate, thus lowering Orange II degradation efficiency.

The kinetics of Orange II degradation was also investigated at different temperatures (25, 35, 45, and 55 °C), and the results are shown in Figure 7d. It was found that Orange II degradation in the Mn_3O_4−rGO/PMS system is well formulated by a pseudosecond-order kinetics.[51,52] The k_{obs} values of Orange II degradation were found to be 0.383 (R^2 = 0.936) at 25 °C, 0.793 (R^2 = 0.978) at 35 °C, 1.22 (R^2 = 0.991) at 45 °C, and 2.52 L mg^{-1} min^{-1} (R^2 = 0.953), respectively (Table 1), suggesting that increased temperature

Table 1. Kinetic Rate Constants and Activation Energy of Mn_3O_4−rGO/PMS in Oxidation of Orange II

T, °C	k_{obs} × 10^3 (L mg^{-1} min^{-1})	R^2 of k_{obs}	ΔE (kJ mol^{-1})	R^2 of ΔE
25	0.383	0.936	49.5	0.99
35	0.793	0.978		
45	1.22	0.991		
55	2.52	0.953		

could significantly increase the Orange II removal rate. The activation energy (E_a) of the reaction on the Mn_3O_4−rGO surface was then obtained to be 49.5 kJ mol^{-1} by plotting ln(k_{obs}) against 1/T (inset Figure 8) on the basis of the Arrhenius equation. This value is higher than the activation energy of the diffusion-controlled reactions, which is usually within 10−13 kJ mol^{-1}, implying that the apparent reaction rate

dx.doi.org/10.1021/ie303220x | Ind. Eng. Chem. Res. 2013, 52, 3637−3645

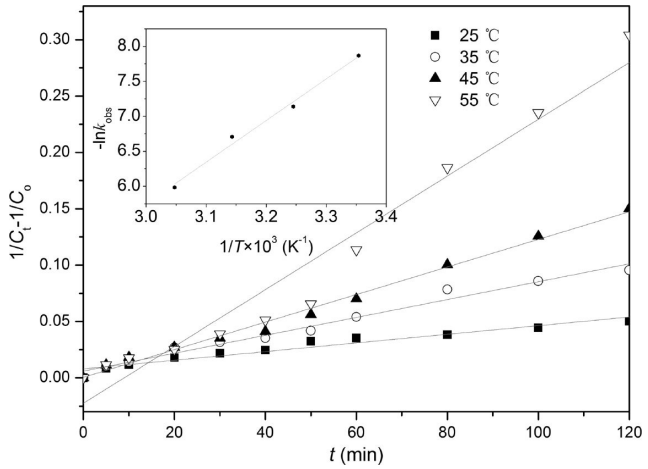

Figure 8. $1/C_t - 1/C_o$ versus reaction time based on the effect of reaction temperature. Inset indicates the Arrhenius curve (reaction conditions: [Orange II] = 60 mg/L, [PMS] = 0.3 g/200 mL, [catalyst] = 10 mg/200 mL).

for this process is dominated by the rate of intrinsic chemical reactions on the oxide surface rather than the rate of mass transfer.[53] The activation energies of the reactions using different heterogeneous catalysts from literatures are between 15.8 and 75.5 kJ mol^{-1}, for example, 15.8 kJ mol^{-1} on $CoFe_2O_4$–graphene,[25] 26.5 kJ mol^{-1} on Co_3O_4–graphene,[44] 61.7–75.5 kJ mol^{-1} on Co_3O_4/SiO_2,[54] 69.7 kJ mol^{-1} on Co/ZSM-5,[55] and 59.7 kJ mol^{-1} on Co/AC.[7] Although it is difficult to compare the catalytic activity of various heterogeneous catalysts due to the difference in experimental conditions, all of these results suggest that Mn_3O_4–rGO catalyst is a promising catalytic material for oxidation processes.

3.3. Stability and Reusability of Mn_3O_4–rGO Catalyst. The stability and recyclability of Mn_3O_4–rGO catalyst were evaluated by successive tests of Orange II degradation, as shown in Figure 9. It was found that Mn_3O_4–rGO hybrids were able to be reutilized and the Orange II degradation on the reused catalyst remained almost unchanged in four cycles. XRD measurements showed a similar structure of the catalyst before and after the reaction (Figure 1). Therefore, Mn_3O_4–rGO hybrid has an excellent long-term stability and can be reused without loss of catalytic activity for the degradation of organic pollutants in water, which could be attributed to the stable structure of the Mn_3O_4–rGO.

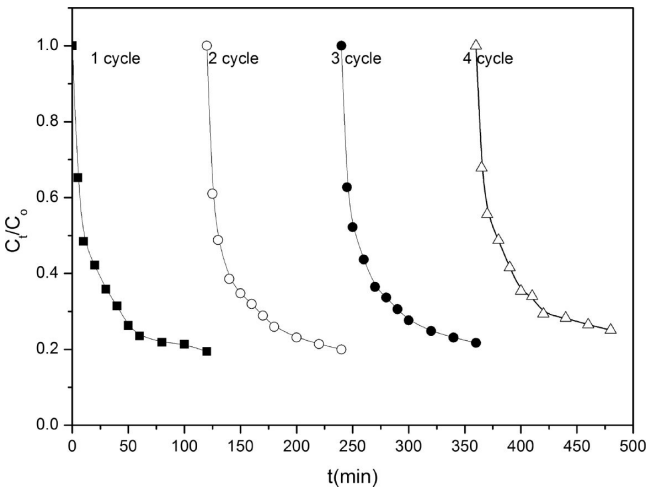

Figure 9. Degradation of Orange II with the recycled Mn_3O_4–rGO hybrids (reaction conditions: [Orange II] = 60 mg/L, [PMS] = 0.30 g/200 mL, [catalyst] = 10 mg/200 mL, pH_i = 7.0, and T = 25 °C).

3.4. Role of Mn_3O_4 and rGO. According to previous studies, the primary radical $SO_4^{-\bullet}$ plays a key role in degradation of Orange II. Mn_3O_4 is believed to be composed of $MnO{\cdot}Mn_2O_3$. The $\equiv Mn^{2+}$ species can react with PMS to generate surface-bound $SO_4^{-\bullet}$ (eq 1), where $\equiv Mn^{2+}$ stands for Mn(II) sites on the catalyst surface. Some more $\equiv Mn^{2+}$ species are produced through the reactions of the formed $\equiv Mn^{3+}$ species with PMS (eq 2). Manganese is capable of redox cycling in the presence of PMS and produces $SO_5^{-\bullet}$ (eqs 1,2), behaving similarly to iron in a Fenton-like reaction.[5356] Finally, Orange II is broken down mainly by $SO_4^{-\bullet}$. The biggest advantage of this system is that the reverse electron transfer from Mn^{3+} to Mn^{2+} is thermodynamically feasible.[57] The regeneration of the catalyst makes the reaction proceed cyclically until PMS is completely consumed at enough reaction time. The reaction mechanism for the degradation of Orange II is shown as follows:[12,58,59]

$$\equiv Mn^{2+} + HSO_5^- \rightarrow \equiv Mn^{3+} + SO_4^{-\bullet} + OH^- \quad (1)$$

$$\equiv Mn^{3+} + HSO_5^- \rightarrow \equiv Mn^{2+} + SO_5^{-\bullet} + H^+ \quad (2)$$

$$2SO_5^{-\bullet} \leftrightarrow {}^-O_3SOOOOSO_3^- \rightarrow \{SO_4^{-\bullet}O_2SO_4^{-\bullet}\} \quad (3)$$

$$\{SO_4^{-\bullet}O_2SO_4^{-\bullet}\} \rightarrow O_2 + S_2O_8^{2-} \quad (4)$$

$$\{SO_4^{-\bullet}O_2SO_4^{-\bullet}\} \rightarrow O_2 + 2SO_4^{-\bullet} \quad (5)$$

$$SO_4^{-\bullet} + \text{Orange II} \rightarrow [\text{...many steps...}] \rightarrow CO_2 + H_2O \quad (6)$$

The excellent catalytic activity of Mn_3O_4–rGO hybrids is probably due to a positive synergistic effects between Mn_3O_4 and graphene.[15] In this investigation, characterizations from SEM (TEM), Raman, and XPS show manganese atoms were covalently attached to graphene sheets through the oxygen groups, and the chemically reduced graphene oxide produced a significant number of chemical defects for oxidation and reactive adsorption. First, BET measurements showed that Mn_3O_4–rGO hybrids have a higher surface area (65.0 m^2/g) than Mn_3O_4 (25.9 m^2/g), resulting in more active sites for adsorption of organic pollutants, and Orange II has the ability to create π–π stacking interactions with the graphene aromatic domains. This adsorption process significantly increases the concentration of the organic molecules near the catalytic surface, which is an important factor for achieving higher catalytic degradation rates.[22] Second, as compared to bare Mn_3O_4 NPs, graphene can offer an environment to prevent aggregation of Mn_3O_4 NPs, and the graphene nanosheets as electron transfer channels make the degradation process occur efficiently on these graphene-based nanomaterial.[60] The improved activity of Mn_3O_4–rGO hybrids for Orange II degradation may be related to the strong interaction (Mn–O–C) between Mn_3O_4 and graphene in the hybrids and good dispersion of Mn_3O_4 NPs.[20,61] The Mn–O–C sites will favor the formation of OH[61] on Mn_3O_4 and promote activation of PMS for $SO_4^{-\bullet}$ production. Third, graphene is not only a support, but also a catalyst for activating Oxone to produce $SO_4^{-\bullet}$, whose reaction mechanism has been reported in other literature.[43] Porous Mn_3O_4–rGO hybrids are expected to make

dx.doi.org/10.1021/ie303220x | Ind. Eng. Chem. Res. 2013, 52, 3637–3645

a significant contribution to the advancement of high catalytic performance because of the low cost associated with the precursor and the simplicity in preparation of this novel structure, and they serve as promising candidates for other applications such as lithium-ion batteries and supercapacitors.

4. CONCLUSION

Mn_3O_4−rGO hybrids were prepared under basic conditions, characterized by FESEM, TEM, EDS, XRD, FTIR, and TGA techniques and used for the degradation of Orange II in aqueous solutions. TEM observations indicate that graphene sheets are fully exfoliated and decorated with Mn_3O_4 NPs at an average size of 29.2 nm. The catalytic performance showed that coupling Mn_3O_4 NPs with graphene sheets leads to higher catalytic activity for the degradation of Orange II than pure Mn_3O_4, attributed to the roles of rGO in NPs dispersion and activation of PMS. Orange II degradation in the Mn_3O_4−rGO/PMS system follows the pseudosecond-order kinetics, and the activation energy is 49.5 kJ/mol. The rate constant of Orange II degradation was found to increase with increasing temperature and Oxone dosage, but to decrease with increasing initial Orange II concentration. Mn_3O_4−rGO hybrids exhibited stable performance and are thus believed to be effective catalytic materials for environmental applications.

AUTHOR INFORMATION

Corresponding Author

*Tel.: +86 551 2901458 (Y.Y.); +61 8 9266 3776 (S.W.). Fax: +86 551 2901450 (Y.Y.); +61 8 9266 2681 (S.W.). E-mail: yaoyunjin@gmail.com (Y.Y.); shaobin.wang@curtin.edu.au (S.W.).

Notes

The authors declare no competing financial interest.

ACKNOWLEDGMENTS

This work was supported by the National Natural Science Foundation of China (Grants 20976033 and 21176054), the Anhui Provincial Natural Science Foundation (no. 1308085MB21), the Fundamental Research Funds for the Central Universities (no. 2012HGQC0010), and the Innovative Foundation Project for Students of Hefei University of Technology (no. 2012CXCY267).

REFERENCES

(1) Gupta, V. K.; Ali, I.; Saleh, T. A.; Nayak, A.; Agarwal, S. Chemical treatment technologies for waste-water recycling-an overview. *RSC Adv.* **2012**, *2*, 6380−6388.

(2) Gupta, V. K.; Srivastava, S. K.; Tyagi, R. Design parameters for the treatment of phenolic wastes by carbon columns (obtained from fertilizer waste material). *Water Res.* **2000**, *34*, 1543−1550.

(3) Han, Y.-F.; Chen, F.; Ramesh, K.; Zhong, Z.; Widjaja, E.; Chen, L. Preparation of nanosized Mn_3O_4/SBA-15 catalyst for complete oxidation of low concentration EtOH in aqueous solution with H_2O_2. *Appl. Catal., B* **2007**, *76*, 227−234.

(4) Wang, Y.; Zhao, H.; Gao, J.; Zhao, G.; Zhang, Y.; Zhang, Y. Rapid mineralization of azo-dye wastewater by microwave synergistic electro-fenton oxidation process. *J. Phys. Chem. C* **2012**, *116*, 7457−7463.

(5) Tušar, N. N.; Maučec, D.; Rangus, M.; Arčon, I.; Mazaj, M.; Cotman, M.; Pintar, A.; Kaučič, V. Manganese functionalized silicate nanoparticles as a fenton-type catalyst for water purification by advanced oxidation processes (AOP). *Adv. Funct. Mater.* **2012**, *22*, 820−826.

(6) Yuan, S.; Fan, Y.; Zhang, Y.; Tong, M.; Liao, P. Pd-catalytic in situ generation of H_2O_2 from H_2 and O_2 produced by water electrolysis for the efficient electro-fenton degradation of rhodamine B. *Environ. Sci. Technol.* **2011**, *45*, 8514−8520.

(7) Shukla, P. R.; Wang, S.; Sun, H.; Ang, H. M.; Tadé, M. Activated carbon supported cobalt catalysts for advanced oxidation of organic contaminants in aqueous solution. *Appl. Catal., B* **2010**, *100*, 529−534.

(8) Lente, G. b.; Kalmár, J. z.; Baranyai, Z.; Kun, A. z.; Kék, I.; Bajusz, D. v.; Takács, M.; Veres, L.; Fábián, I. n. One-versus two-electron oxidation with peroxomonosulfate ion: Reactions with iron(II), vanadium(IV), halide ions, and photoreaction with cerium(III). *Inorg. Chem.* **2009**, *48*, 1763−1773.

(9) Chen, X.; Chen, J.; Qiao, X.; Wang, D.; Cai, X. Performance of nano-Co_3O_4/peroxymonosulfate system: kinetics and mechanism study using Acid Orange 7 as a model compound. *Appl. Catal., B* **2008**, *80*, 116−121.

(10) Chan, K. H.; Chu, W. Degradation of atrazine by cobalt-mediated activation of peroxymonosulfate: Different cobalt counter-anions in homogenous process and cobalt oxide catalysts in photolytic heterogeneous process. *Water Res.* **2009**, *43*, 2513−2521.

(11) Zhang, W.; Tay, H. L.; Lim, S. S.; Wang, Y.; Zhong, Z.; Xu, R. Supported cobalt oxide on MgO: Highly efficient catalysts for degradation of organic dyes in dilute solutions. *Appl. Catal., B* **2010**, *95*, 93−99.

(12) Yang, Q.; Choi, H.; Al-Abed, S. R.; Dionysiou, D. D. Iron−cobalt mixed oxide nanocatalysts: Heterogeneous peroxymonosulfate activation, cobalt leaching, and ferromagnetic properties for environmental applications. *Appl. Catal., B* **2009**, *88*, 462−469.

(13) Liang, H.; Sun, H.; Patel, A.; Shukla, P.; Zhu, Z. H.; Wang, S. Excellent performance of mesoporous Co_3O_4/MnO_2 nanoparticles in heterogeneous activation of peroxymonosulfate for phenol degradation in aqueous solutions. *Appl. Catal., B* **2012**, *127*, 330−335.

(14) Saputra, E.; Muhammad, S.; Sun, H.; Patel, A.; Shukla, P.; Zhu, Z. H.; Wang, S. α-MnO_2 activation of peroxymonosulfate for catalytic phenol degradation in aqueous solutions. *Catal. Commun.* **2012**, *26*, 144−148.

(15) Wang, D.; Li, Y.; Wang, Q.; Wang, T. Facile synthesis of porous Mn_3O_4 nanocrystal−graphene nanocomposites for electrochemical supercapacitors. *Eur. J. Inorg. Chem.* **2012**, *2012*, 628−635.

(16) Chen, Z.; Jiao, Z.; Pan, D.; Li, Z.; Wu, M.; Shek, C.-H.; Wu, C. M. L.; Lai, J. K. L. Recent advances in manganese oxide nanocrystals: fabrication, characterization, and microstructure. *Chem. Rev.* **2012**, *112*, 3833−3855.

(17) Zhu, J.; He, J. Facile synthesis of graphene-wrapped honeycomb MnO_2 nanospheres and their application in supercapacitors. *ACS Appl. Mater. Interfaces* **2012**, *4*, 1770−1776.

(18) Yao, Y.; Miao, S.; Liu, S.; Ma, L. P.; Sun, H.; Wang, S. Synthesis, characterization, and adsorption properties of magnetic Fe_3O_4@ graphene nanocomposite. *Chem. Eng. J.* **2012**, *184*, 326−332.

(19) Choi, W.; Lahiri, I.; Seelaboyina, R.; Kang, Y. S. Synthesis of graphene and its applications: A review. *Crit. Rev. Solid State Mater. Sci.* **2010**, *35*, 52−71.

(20) Zhang, Q.; Tian, C.; Wu, A.; Tan, T.; Sun, L.; Wang, L.; Fu, H. A facile one-pot route for the controllable growth of small sized and well-dispersed ZnO particles on GO-derived graphene. *J. Mater. Chem.* **2012**, *22*, 11778−11784.

(21) Li, B.; Cao, H. ZnO@graphene composite with enhanced performance for the removal of dye from water. *J. Mater. Chem.* **2011**, *21*, 3346−3349.

(22) Perera, S. D.; Mariano, R. G.; Vu, K.; Nour, N.; Seitz, O.; Chabal, Y.; Balkus, K. J. Hydrothermal synthesis of graphene-TiO_2 nanotube composites with enhanced photocatalytic activity. *ACS Catal.* **2012**, *2*, 949−956.

(23) Pan, X.; Zhao, Y.; Liu, S.; Korzeniewski, C. L.; Wang, S.; Fan, Z. Comparing graphene-TiO_2 nanowire and graphene-TiO_2 nanoparticle composite photocatalysts. *ACS Appl. Mater. Interfaces* **2012**, *4*, 3944−3950.

(24) Fu, Y.; Chen, H.; Sun, X.; Wang, X. Graphene-supported nickel ferrite: A magnetically separable photocatalyst with high activity under visible light. *AIChE J.* **2012**, *58*, 3298−3305.

(25) Yao, Y.; Yang, Z.; Zhang, D.; Peng, W.; Sun, H.; Wang, S. Magnetic $CoFe_2O_4$-graphene hybrids: Facile synthesis, characterization and catalytic properties. *Ind. Eng. Chem. Res.* **2012**, *51*, 6044−6051.
(26) Li, L.; Guo, Z.; Du, A.; Liu, H. Rapid microwave-assisted synthesis of Mn_3O_4-graphene nanocomposite and its lithium storage properties. *J. Mater. Chem.* **2012**, *22*, 3600−3605.
(27) Zhang, X.; Sun, X.; Chen, Y.; Zhang, D.; Ma, Y. One-step solvothermal synthesis of graphene/Mn_3O_4 nanocomposites and their electrochemical properties for supercapacitors. *Mater. Lett.* **2012**, *68*, 336−339.
(28) Lee, J. W.; Hall, A. S.; Kim, J.-D.; Mallouk, T. E. A facile and template-free hydrothermal synthesis of Mn_3O_4 nanorods on graphene sheets for supercapacitor electrodes with long cycle stability. *Chem. Mater.* **2012**, *24*, 1158−1164.
(29) Hartono, T.; Wang, S.; Ma, Q.; Zhu, Z. Layer structured graphite oxide as a novel adsorbent for humic acid removal from aqueous solution. *J. Colloid Interface Sci.* **2009**, *333*, 114−119.
(30) Bradder, P.; Ling, S. K.; Wang, S.; Liu, S. Dye adsorption on layered graphite oxide. *J. Chem. Eng. Data* **2011**, *56*, 138−141.
(31) Yao, Y.; Miao, S.; Yu, S.; Ping, Ma. L.; Sun, H.; Wang, S. Fabrication of Fe_3O_4/SiO_2 core/shell nanoparticles attached to graphene oxide and its use as an adsorbent. *J. Colloid Interface Sci.* **2012**, *379*, 20−26.
(32) Chandra, V.; Park, J.; Chun, Y.; Lee, J. W.; Hwang, I.-C.; Kim, K. S. Water-dispersible magnetite-reduced graphene oxide composites for arsenic removal. *ACS Nano* **2010**, *4*, 3979−3986.
(33) Li, B.; Cao, H.; Shao, J.; Li, G.; Qu, M.; Yin, G. Co_3O_4@graphene composites as anode materials for high-performance lithium ion batteries. *Inorg. Chem.* **2011**, *50*, 1628−1632.
(34) Wang, P.; Yang, S.; Shan, L.; Niu, R.; Shao, X. Involvements of chloride ion in decolorization of Acid Orange 7 by activated peroxydisulfate or peroxymonosulfate oxidation. *J. Environ. Sci.* **2011**, *23*, 1799−1807.
(35) Anipsitakis, G. P.; Dionysiou, D. D. Degradation of organic contaminants in Water with sulfate radicals generated by the conjunction of peroxymonosulfate with cobalt. *Environ. Sci. Technol.* **2003**, *37*, 4790−4797.
(36) Li, X.; Wang, X.; Song, S.; Liu, D.; Zhang, H. Selectively deposited noble metal nanoparticles on Fe_3O_4/graphene composites: Stable, recyclable, and magnetically separable catalysts. *Chem.-Eur. J.* **2012**, *18*, 7601−7607.
(37) Jiang, H. G.; Ruhle, M.; Lavernia, E. J. On the applicability of the X-ray diffraction line profile analysis in extracting grain size and microstrain in nanocrystalline materials. *J. Mater. Res.* **1999**, *14*, 549−559.
(38) Kim, H.; Seo, D.-H.; Kim, S.-W.; Kim, J.; Kang, K. Highly reversible Co_3O_4/graphene hybrid anode for lithium rechargeable batteries. *Carbon* **2011**, *49*, 326−332.
(39) Wang, W.-S.; Wang, D.-H.; Qu, W.-G.; Lu, L.-Q.; Xu, A.-W. Large ultrathin anatase TiO_2 nanosheets with exposed {001} facets on graphene for enhanced visible light photocatalytic activity. *J. Phys. Chem. C* **2012**, *116*, 19893−19901.
(40) Hou, Y.; Cheng, Y.; Hobson, T.; Liu, J. Design and synthesis of hierarchical MnO_2 nanospheres/carbon nanotubes/conducting polymer ternary composite for high performance electrochemical electrodes. *Nano Lett.* **2010**, *10*, 2727−2733.
(41) Zhang, J.; Jiang, J.; Zhao, X. S. Synthesis and capacitive properties of manganese oxide nanosheets dispersed on functionalized graphene sheets. *J. Phys. Chem. C* **2011**, *115*, 6448−6454.
(42) Wang, J.; Zheng, S.; Shao, Y.; Liu, J.; Xu, Z.; Zhu, D. Amino-functionalized Fe_3O_4@SiO_2 core-shell magnetic nanomaterial as a novel adsorbent for aqueous heavy metals removal. *J. Colloid Interface Sci.* **2010**, *349*, 293−299.
(43) Sun, H.; Liu, S.; Zhou, G.; Ang, H. M.; Tadé, M. O.; Wang, S. Reduced graphene oxide for catalytic oxidation of aqueous organic pollutants. *ACS Appl. Mater. Interfaces* **2012**, *4*, 5466−5471.
(44) Yao, Y.; Yang, Z.; Sun, H.; Wang, S. Hydrothermal synthesis of Co_3O_4-Graphene for heterogeneous activation of peroxymonosulfate for decomposition of phenol. *Ind. Eng. Chem. Res.* **2012**, *51*, 14958−14965.
(45) Fu, Y.; Xiong, P.; Chen, H.; Sun, X.; Wang, X. High photocatalytic activity of magnetically separable manganese ferrite−graphene heteroarchitectures. *Ind. Eng. Chem. Res.* **2011**, *51*, 725−731.
(46) Long, X.; Yang, Z.; Wang, H.; Chen, M.; Peng, K.; Zeng, Q.; Xu, A. Selective degradation of orange II with the cobalt(II)−bicarbonate−hydrogen peroxide system. *Ind. Eng. Chem. Res.* **2012**, *51*, 11998−12003.
(47) Wang, Z. H.; Yuan, R. X.; Guo, Y. G.; Xu, L.; Liu, J. S. Effects of chloride ions on bleaching of azo dyes by Co^{2+}/oxone regent: Kinetic analysis. *J. Hazard. Mater.* **2011**, *190*, 1083−1087.
(48) Guan, Y.-H.; Ma, J.; Li, X.-C.; Fang, J.-Y.; Chen, L.-W. Influence of pH on the formation of sulfate and hydroxyl radicals in the UV/peroxymonosulfate system. *Environ. Sci. Technol.* **2011**, *45*, 9308−9314.
(49) Zhu, Y.; Chen, S.; Quan, X.; Zhang, Y. Cobalt implanted TiO_2 nanocatalyst for heterogeneous activation of peroxymonosulfate. *RSC Adv.* **2013**, *3*, 520−525.
(50) Liang, C.; Su, H.-W. Identification of sulfate and hydroxyl radicals in thermally activated persulfate. *Ind. Eng. Chem. Res.* **2009**, *48*, 5558−5562.
(51) Meeks, N. D.; Smuleac, V.; Stevens, C.; Bhattacharyya, D. Iron-based nanoparticles for toxic organic degradation: Silica platform and green synthesis. *Ind. Eng. Chem. Res.* **2012**, *51*, 9581−9590.
(52) De Laat, J.; Gallard, H. Catalytic decomposition of hydrogen peroxide by Fe(III) in homogeneous aqueous solution: Mechanism and kinetic modeling. *Environ. Sci. Technol.* **1999**, *33*, 2726−2732.
(53) Xu, L.; Wang, J. Magnetic nanoscaled Fe_3O_4/CeO_2 composite as an efficient Fenton-like heterogeneous catalyst for degradation of 4-chlorophenol. *Environ. Sci. Technol.* **2012**, *46*, 10145−10153.
(54) Shukla, P.; Sun, H.; Wang, S.; Ang, H. M.; Tadé, M. O. Nanosized Co_3O_4/SiO_2 for heterogeneous oxidation of phenolic contaminants in waste water. *Sep. Purif. Technol.* **2011**, *77*, 230−236.
(55) Shukla, P.; Wang, S.; Singh, K.; Ang, H. M.; Tadé, M. O. Cobalt exchanged zeolites for heterogeneous catalytic oxidation of phenol in the presence of peroxymonosulphate. *Appl. Catal., B* **2010**, *99*, 163−169.
(56) Heckert, E. G.; Seal, S.; Self, W. T. Fenton-like reaction catalyzed by the rare earth inner transition metal cerium. *Environ. Sci. Technol.* **2008**, *42*, 5014−5019.
(57) Guo, W.; Su, S.; Yi, C.; Ma, Z. Degradation of antibiotics amoxicillin by Co_3O_4-catalyzed peroxymonosulfate system. *Environ. Prog. Sustainable Energy* **2012**, DOI: 10.1002/ep.10633.
(58) Anipsitakis, G. P.; Dionysiou, D. D.; Gonzalez, M. A. Cobalt-mediated activation of peroxymonosulfate and sulfate radical attack on phenolic compounds. implications of chloride ions. *Environ. Sci. Technol.* **2006**, *40*, 1000−1007.
(59) Yuan, R.; Ramjaun, S. N.; Wang, Z.; Liu, J. Effects of chloride ion on degradation of Acid Orange 7 by sulfate radical-based advanced oxidation process: Implications for formation of chlorinated aromatic compounds. *J. Hazard. Mater.* **2011**, *196*, 173−179.
(60) Ji, Z.; Shen, X.; Zhu, G.; Zhou, H.; Yuan, A. Reduced graphene oxide/nickel nanocomposites: facile synthesis, magnetic and catalytic properties. *J. Mater. Chem.* **2012**, *22*, 3471−3477.
(61) Mabayoje, O.; Seredych, M.; Bandosz, T. J. Cobalt (hydr)oxide/graphite oxide composites: Importance of surface chemical heterogeneity for reactive adsorption of hydrogen sulfide. *J. Colloid Interface Sci.* **2012**, *378*, 1−9.